The Utility of Direct-Current as Compared to Frequency Domain Measurements in Spectrally-Constrained Diffuse Optical Tomography Toward Cancer Imaging

www.tcrt.org

Guan Xu[1]
Daqing Piao, Ph.D.[1]*
Hamid Dehghani, Ph.D.[2]

[1]School of Electrical and Computer Engineering, Oklahoma State University, Stillwater, OK, USA

[2]School of Computer Science, The University of Birmingham, Birmingham, UK

This work investigates, by means of analytical and simulation studies, the performance of spectrally-constrained image reconstruction in Continuous-Wave or Direct-Current (DC) and Frequency Domain (FD) near-infrared optical tomography. A recent analytic approach for estimating the accuracy of target recovery and the level of background artifact for optical tomography at single wavelength, based on the analysis of parametric reconstruction uncertainty level (PRUL), is extended to spectrally-constrained optical tomography. The analytical model is implemented to rank three sets of wavelengths that had been used as spectral *prior* in an independent experimental study. Subsequent simulation appraises the recovery of oxygenated hemoglobin (HbO), deoxygenated hemoglobin (Hb), water (H_2O), scattering amplitude (*A*), and scattering power (*b*) using DC-only, DC-excluded FD, and DC-included FD, based on the three sets of wavelengths as the spectral *prior*. The simulation results support the analytic ranking of the performance of the three sets of spectral *priors*, and generally agree with the performance outcome of DC-only versus that of DC-excluded FD and DC-included FD. Specifically, this study indicate that: 1) the rank of overall quality of chromophore recovery is Hb, H_2O, and HbO from the highest to lowest; and in the scattering part the *A* is always better recovered than *b*. This outcome does suggest that the DC-only information gives rise to unique solution to the image reconstruction routine under the given spectral *prior*. 2) DC-information is not-redundant in FD-reconstruction, as the artifact levels of DC-included FD reconstruction are always lower than those of DC-excluded FD. 3) The artifact level as represented by the noise-to-contrast-ratio is almost always the lowest in DC-only, leading to generally better resolution of multiple targets of identical contrasts over the background than in FD. However, the FD could outperform DC in the recovery of scattering properties including both *A* and *b* when the spectral *prior* is less optimal, implying the benefit of phase-information in scattering recovery in the context of spectrally-constrained optical tomography.

Key words: Optical tomography; Image reconstruction; Spectral *prior*; Frequency-domain; Continuous-wave.

Introduction

Multi-spectral near infrared optical tomography aims to reconstruct pathologically-relevant optical heterogeneities in biological tissue from information

---

Abbreviations: Diffuse Optical Tomography (DOT); Parametric Reconstruction Uncertainty Level (PRUL); Direct-Current (DC); Continuous-Wave (CW); Frequency Domain (FD); Alternate Current (AC); PHase Shift (PHS); Contrast to Noise Ratio (CNR); Noise to Contrast Ratio (NCR); Oxygenated Hemoglobin (HbO); Deoxygenated Hemoglobin (Hb).

*Corresponding author:
Dr. Daqing Piao, Ph.D.
E-mail: daqing.piao@okstate.edu

obtained over a spectrum of light (1-5). The technique utilizes measurements at multiple wavelengths (5) to decompose the spectrally variant tissue optical properties such as absorption and reduced scattering coefficients into spectrally invariant chromophore concentrations and spectrally insensitive scattering properties such as scattering power and scattering amplitude (2). Although discussions remain over the uniqueness of optical tomography reconstruction by single wavelength Continuous-Wave (CW) or Direct-Current (DC) measurements (6-7), the unique solution to optical tomography reconstruction based on spectrally-constrained DC measurement has been demonstrated by Corlu *et al.* (2). Further studies based on DC measurements have been reported for imaging of breast (2-3, 8-9), prostate (10), brain function (11), small animal (12), *etc.*, and the spectrally-constrained DC-based reconstruction is shown to be more robust than the spatially-constrained single-wavelength DC-based reconstruction in recovering the optical heterogeneities (13). In recent studies (14-15), Wang *et al.* implemented broadband frequency domain (FD) measurements to multispectral optical tomography reconstruction. The studies concluded that increasing the bandwidth of FD measurements improves reconstruction results. In their subsequent studies, Wang *et al.* integrated the FD detection with DC (16-17) measurements to further expand the effective spectral bandwidth for reconstruction. The successful outcome of such FD/DC complemented approach, nonetheless, underlines a more fundamental inquiry, that is, under the same spectral-constraint, how DC based reconstruction performs with respect to FD based reconstruction. Intuitively, one might expect FD reconstruction to outperform DC reconstruction in all aspects owing to the extra phase information. However, such consideration has neither been confirmed nor negated, for which direct comparison of DC and FD reconstructions under the same context of spectral-constraint is necessary. For non-spectrally-constrained optical tomography, or optical tomography at single-wavelength, our previous study (18) investigated three conditions of reconstruction: 1) DC-only; 2) DC-excluded FD, *i.e.* utilizing only the modulation amplitude (AC) and phase shift (PHS); and 3) DC-included FD, *i.e.* including DC, AC and PHS. It is revealed that the DC-only reconstruction, despite the less accurate estimation of the target optical properties, presents higher Contrast-to-Noise-Ratio (CNR) than the FD reconstruction does, thereby potentially better resolves the targets in certain noisy circumferences. It is also demonstrated that with spatial-*prior*, DC-only reconstruction is essentially equivalent to FD reconstructions, and without spatial-*prior*, DC-included FD reconstruction generally outperforms DC-excluded FD reconstruction. Will spectrally-constrained reconstruction have similar outcome?

The study in (18) introduced an analytic model to estimate the translation of uncertainties in the measurements to the uncertainties in the reconstructed images, namely parameter-recovery-uncertainty-level (PRUL). This current study aims to evaluate the PRULs in spectrally-constrained optical tomography reconstruction. Specifically, we explore the PRULs of the concentrations of several important NIR chromophores, including oxygenated hemoglobin (HbO), deoxygenated hemoglobin (Hb), and water, and scattering parameters such as scattering amplitude and scattering power. The PRUL analyses are for the measurements of DC-only, DC-excluded FD, and DC-included FD, as did with the study in (18), even though other configurations of DC/FD measurements could be employed (19). The PRUL analyses are, essentially, to quantify the gradients of the chromophore concentrations and scattering components with respect to DC or FD measurement components. This study seeks to derive the wavelength-specific gradients of the chromophore concentrations and scattering components with respect to the optical properties in DC or FD measurements, which are then to be integrated with the gradients of the optical properties with respect to DC or FD measurements previously analyzed in (18) to reach the complete expressions of PRULs in multi-spectral measurements.

A practical issue arises in spectrally-constrained optical tomography is the selection of optimal set of wavelengths given the choices of doing so in the system integration. The optimization approaches demonstrated by Corlu *et al.* (2, 8) and Eames *et al.* (20) are similar as both methods compare the residue and condition numbers of numerically approximated sensitivity matrices derived for each set of the wavelength combinations. This current work proposes a novel method of optimizing the wavelength selection for spectrally-constrained optical tomography reconstruction based on the PRUL analyses. As the gradients in PRULs are formatively equivalent to the sensitivity matrices, the new method is shown to optimize the wavelength selection as effectively as Corlu's and Eames' methods do, but at much lower computational load.

The PRUL analyses under spectral-constraint as well as the newly proposed method for spectral-*prior* optimization are examined by synthetic studies in a 2-dimensional circular imaging geometry resembling an applicator enclosing the medium (3, 20). The synthetic studies are to recover targets each of which possesses only one independent contrast, and to resolve two closely positioned targets of identical studied properties. Evaluation criteria include the recovered target properties and the noise-to-contrast-ratio (NCR). In this study, NCR is defined as, opposed to CNR, the absolute levels of the background artifacts normalized by the target-to-background contrast, therefore a lower NCR is preferred.

It is well-known that multi-spectral optical tomography reconstruction can be implemented in two ways. A conventional

"indirect" method first reconstructs wavelength-specific absorption and scattering distributions and then deduces the chromophore concentrations and scattering components (9). While a "direct" spectrally-constraint method integrates the spectral information into the sensitivity matrices to directly recover the chromophore concentrations and scattering parameters (2-4, 8, 13-14, 20-22). Note that the efficacies of both methods are ultimately bounded by the determination of the gradient of the spectrally variant optical properties with respect to the chromophore concentrations and scattering parameters. However, as the direct method has less unknown values than the indirect method does, the inverse problem in the direct method is better conditioned. Therefore it is well expected (2-4, 8, 13, 21) that the direct method outperforms the indirect method in terms of CNR and inter-parameter cross-talk, should the amount of the wavelengths be sufficient for recovering the unknown parameters. In light of this, the "direct" reconstruction method is adopted in the simulations of this study for multi-spectral optical tomography reconstruction.

The rest of the paper is structured to the following sections for the comparison of DC, DC-excluded FD, and DC-included FD measurements under the same spectral-constraint: analytical derivation of the PRULs, numerical implementation of the derived PRULs, ranking of the spectral-*priors* being implemented for the PRUL analyses, and finite-element-based simulation to validate the preceding numerical evaluations. The simulation study will demonstrate that: 1) the ranking of the wavelength sets given by the analytical approach is correct; 2) the rankings of the overall quality of chromophore recovery and the scattering property given by the analytical approach are correct; 3) DC-information is not-redundant in FD-reconstruction; 4) for less desirable spectral *prior,* the phase in FD gives more robust recovery of the scattering properties.

Parameter Recovery Uncertainty Level (PRUL) in Multi-spectral Measurement

General Expression of the PRUL

For a field point at a distance d from the source in an infinite homogenous diffusive medium, we define $U_{DC}(d, \lambda)$, $U_{AC}(d, \lambda)$ and $\Phi(d, \lambda)$ as the wavelength-specific DC, AC and phase measurands. For two field points located d_1 and d_2 from the source, the differences in their DC, AC, and phase-shift denoted by $\delta(\lambda)$, $a(\lambda)$ and $\varphi(\lambda)$, respectively, can be expressed as (18, 19):

$$\delta(\lambda) = \ln\left(\frac{d_2}{d_1} \frac{U_{DC}(d_2, \lambda)}{U_{DC}(d_1, \lambda)}\right) = -\rho \cdot \sqrt{\frac{\mu_a(\lambda)}{D(\lambda)}} = -\rho \cdot k_{DC} \quad \text{[1-DC]}$$

$$a(\lambda_i) = \ln\left(\frac{d_2}{d_1} \frac{U_{AC}(d_2, \lambda)}{U_{AC}(d_1, \lambda)}\right)$$

$$= -\rho \cdot \sqrt{\frac{\mu_a(\lambda)}{2D(\lambda)}\left(\sqrt{1 + \frac{\omega^2}{v^2 \mu_a^2(\lambda)}} + 1\right)} = -\rho \cdot k_{AC} \quad \text{[1-AC]}$$

$$\phi(\lambda) = \Phi(d_2, \lambda) - \Phi(d_1, \lambda)$$

$$= \rho \cdot \sqrt{\frac{\mu_a(\lambda)}{2D(\lambda)}\left(\sqrt{1 + \frac{\omega^2}{v^2 \mu_a^2(\lambda)}} - 1\right)} = \rho \cdot k_{PHS} \quad \text{[1-PHS]}$$

where $\rho = |d_1 - d_2|$, ω is the angular modulation frequency, v is the speed of light in the medium, and

$$\mu_a(\lambda) = \sum_i \log(10)\varepsilon_i(\lambda) c_i \text{ (the "log" denotes the}$$
$$\text{natural logarithm)} \quad \text{[2-}\mu_a\text{]}$$

$$\mu_s'(\lambda) = A\lambda^{-b} \quad \text{[2-}\mu_s'\text{]}$$

$$D(\lambda) = \{3[\mu_a(\lambda) + \mu_s'(\lambda)]\}^{-1} \quad \text{[2-}D\text{]}$$

are the absorption, reduced scattering and diffusion coefficients of the medium, respectively. In equation [2], $\varepsilon_i(\lambda)$ is the extinction coefficient of chromophore i at wavelength λ (23), A is the scattering amplitude and b is the scattering power (3, 8).

The standard deviations, denoted by σ_δ, σ_a and σ_φ, respectively, of the differences of the measurands δ, a and φ, in fact represent the measurement uncertainties (18, 19). The translation of the measurement uncertainties into variations in the reconstructed spectrally-constrained optical properties may be modeled by

$$\sigma_{x_j} = \sqrt{\left(\frac{\partial x_j}{\partial M(\lambda)}\right)^2 \cdot \sigma_{M(\lambda)}^2}$$

$$= \left|\frac{\partial x_j}{\partial \mu(\lambda)} \cdot \frac{\partial \mu(\lambda)}{\partial M(\lambda)}\right| \cdot \sigma_{M(\lambda)} = \left|\frac{\partial x_j}{\partial \mu(\lambda)}\right| \cdot \sigma_{\mu(\lambda)} \quad \text{[3]}$$

where x represents the set of chromophore concentrations, scattering amplitude and scattering power, M represents the set of δ, a and φ, and $\mu(\lambda)$ represents the set of absorption and reduced scattering coefficients. Note that the $\sigma_{\mu(\lambda)}$ has already been given in Tables II and IV of (18), so only $\partial x/\partial \mu$ needs to be derived in this study.

The PRULs of Chromophore Concentration

By expressing equation [2-μ_a] in matrix form as following:

$$\begin{bmatrix} \mu_a(\lambda_1) \\ \mu_a(\lambda_2) \\ \vdots \\ \mu_a(\lambda_m) \end{bmatrix}_{m\times 1} = \log(10)\cdot \begin{bmatrix} \varepsilon_1(\lambda_1) & \varepsilon_2(\lambda_1) & \dots & \varepsilon_n(\lambda_1) \\ \varepsilon_1(\lambda_2) & \varepsilon_2(\lambda_2) & \dots & \varepsilon_n(\lambda_2) \\ \vdots & \vdots & \ddots & \vdots \\ \varepsilon_1(\lambda_m) & \varepsilon_2(\lambda_m) & \dots & \varepsilon_n(\lambda_m) \end{bmatrix}_{m\times n} \times \begin{bmatrix} C_1 \\ C_2 \\ \vdots \\ C_n \end{bmatrix}_{n\times 1}$$ [4]

one has the gradient of chromophore concentration with respect to the absorption coefficients as:

$$\frac{\partial \bar{c}_{n\times 1}}{\partial (\bar{\mu}_a)_{m\times 1}} = \log^{-1}(10)\cdot \left[(\bar{\varepsilon}^T)_{n\times m} \bar{\varepsilon}_{m\times n} \right]^{-1} (\bar{\varepsilon}^T)_{n\times m}$$

$$= \begin{bmatrix} \dfrac{\partial c_1}{\partial \mu_a(\lambda_1)} & \dfrac{\partial c_1}{\partial \mu_a(\lambda_2)} & \cdots & \dfrac{\partial c_1}{\partial \mu_a(\lambda_m)} \\ \dfrac{\partial c_2}{\partial \mu_a(\lambda_1)} & \dfrac{\partial c_2}{\partial \mu_a(\lambda_2)} & \cdots & \dfrac{\partial c_2}{\partial \mu_a(\lambda_m)} \\ \vdots & \vdots & \ddots & \vdots \\ \dfrac{\partial c_n}{\partial \mu_a(\lambda_1)} & \dfrac{\partial c_n}{\partial \mu_a(\lambda_2)} & \cdots & \dfrac{\partial c_n}{\partial \mu_a(\lambda_m)} \end{bmatrix}_{n\times m}$$ [5]

Combining equation [5] with σ_{μ_a} found in (18), the PRUL of the chromophore concentration becomes:

$$(\bar{\sigma}_c)_{n\times 1} = \left| \frac{\partial \bar{c}_{n\times 1}}{\partial (\bar{\mu}_a)_{m\times 1}} \right|_{n\times m} \cdot \left(\bar{\sigma}_{\mu_a(\lambda)} \right)_{m\times 1}$$ [6]

The PRULs of Scattering Amplitude and Scattering Power

Take the logarithm of equation [2-μ_s'] as

$$\log \mu_s' = \log A + (-b)\log \lambda$$ [7]

and convert equation [7] to the matrix form of:

$$\begin{bmatrix} \log[\mu_s'(\lambda_1)] \\ \log[\mu_s'(\lambda_2)] \\ \dots \\ \log[\mu_s'(\lambda_m)] \end{bmatrix}_{m\times 1} = \begin{bmatrix} 1 & \log \lambda_1 \\ 1 & \log \lambda_2 \\ \dots & \dots \\ 1 & \log \lambda_m \end{bmatrix}_{m\times 2} \times \begin{bmatrix} \log A \\ (-b) \end{bmatrix}_{2\times 1}$$ [8]

one has:

$$\left(\frac{\partial \log A}{\partial \log \mu_s'(\lambda_i)} \right)_{1\times m} = \frac{1}{m\sum_{i=1}^{m} \log^2(\lambda_i) - \left[\sum_{i=1}^{m} \log(\lambda_i) \right]^2}$$

$$\times \left(\begin{bmatrix} \sum_{i=1}^{m} \log^2(\lambda_i) - \log(\lambda_1)\sum_{i=1}^{m} \log(\lambda_i) \\ \sum_{i=1}^{m} \log^2(\lambda_i) - \log(\lambda_2)\sum_{i=1}^{m} \log(\lambda_i) \\ \dots \\ \sum_{i=1}^{m} \log^2(\lambda_i) - \log(\lambda_m)\sum_{i=1}^{m} \log(\lambda_i) \end{bmatrix}^T \right)_{1\times m}$$ [9]

$$\left(\frac{\partial b}{\partial \log \mu_s'(\lambda_i)} \right)_{1\times m} = \frac{1}{m\sum_{i=1}^{n} \log^2(\lambda_i) - \left[\sum_{i=1}^{n} \log(\lambda_i) \right]^2}$$

$$\times \left(\begin{bmatrix} \sum_{i=1}^{m} \log(\lambda_i) + m\cdot \log(\lambda_1) \\ \sum_{i=1}^{m} \log(\lambda_i) + m\cdot \log(\lambda_2) \\ \dots \\ \sum_{i=1}^{m} \log(\lambda_i) + m\cdot \log(\lambda_m) \end{bmatrix}^T \right)_{1\times m}$$ [10]

The PRULs of scattering amplitude and scattering power are then expressed by:

$$\sigma_A = \left| \frac{\partial A}{\partial \log A} \cdot \frac{\partial \log A}{\partial \log \mu_s'(\lambda)} \cdot \frac{\partial \log \mu_s'(\lambda)}{\partial \mu_s'(\lambda)} \right| \cdot \sigma_{\mu_s'(\lambda)}$$

$$= A \cdot \left| \frac{\partial \log A}{\partial \log \mu_s'(\lambda)} \right| \cdot \frac{\sigma_{\mu_s'(\lambda)}}{\mu_s'(\lambda)}$$ [11]

$$\sigma_b = \left| \frac{\partial b}{\partial \log \mu_s'(\lambda)} \cdot \frac{\partial \log \mu_s'(\lambda)}{\partial \mu_s'(\lambda)} \right| \cdot \sigma_{\mu_s'(\lambda)}$$

$$= \left| \frac{\partial b}{\partial \log \mu_s'(\lambda)} \right| \cdot \frac{\sigma_{\mu_s'(\lambda)}}{\mu_s'(\lambda)}$$ [12]

where $(\sigma_{\mu s'(\lambda)}/\mu_s'(\lambda))$ was available in (18).

Qualitative Evaluation of the PRULs Between Scattering Amplitude and Scattering Power

A qualitative evaluation of equations [11] and [12] can estimate which one, between scattering amplitude and scattering power, is less prone to measurement uncertainties. Neglecting the common factor $\sigma_{\mu s'(\lambda)}/\mu_s'$ in equations [11] and [12] as well as the equal denominators in equations [9] and [10], only the elements in the $1 \times m$ matrices in equations [9] and [10] are to be compared. Within the NIR spectral range between $0.6\,\mu m$ and $1\,\mu m$, *i.e.*, $\lambda \in [0.6,1]$ with the unit of μm, one has $-1 \leq \log(\lambda_i) \leq 0 \leq \log^2(\lambda_i) \leq 1$ for the first term in each element and thus

$$\sum \log(\lambda_i) < 0 < \sum \log^2(\lambda_i) \qquad [13]$$

For the second terms of $-\log(\lambda_m)\cdot\sum\log(\lambda_i)$ and $m\cdot\log(\lambda_m)$, apparently $m > -\sum\log(\lambda_i) > 0$ and thus

$$m\cdot\log(\lambda_m) < -\log(\lambda_m)\cdot\sum\log(\lambda_i) < 0 \qquad [14]$$

Summing the inequalities [13] and [14] leads to

$$|\sum\log(\lambda_i) + m\cdot\log(\lambda_m)| > |\sum\log^2(\lambda_i) - \log(\lambda_m)\cdot\sum\log(\lambda_i)| \quad [15]$$

which implies that the PRULs of the scattering power should exceed that of scattering amplitude, or the scattering power is more prone to noise than the scattering amplitude is.

Numerical Evaluation of PRULs in Multi-spectral Measurement

Sets of Spectral-prior Used for PRUL Evaluation

We implemented the 3 sets of wavelengths used in (8) as the spectral-*prior* for quantitative analyses of PRULs in multi-spectral measurements. Each of the spectral-*prior* sets contains 5 wavelengths as shown in Figure 1 and Table I. The set

1 expands 186 nm from 740 nm to 926 nm. The set 2 expands 240 nm from 650 nm to 890 nm. The set 3 expands 280 nm, the broadest among the three, from 650 nm to 930 nm. Note that the three wavelength sets are not chosen arbitrarily, in fact, under the caliber introduced in (8) one of them, the set 3, forms an optimal set, so they are considered suitable for demonstrating the prominent cases of spectral-*prior*. Note that the spectra in Figure 1 follow the chromophore absorption spectra used in (2, 8), which are based on the study of Prahl (23).

Criteria of Wavelength Optimization in the Context of Minimizing PRULs

Wavelength optimization for spectrally-constrained optical tomography would naturally reduce the uncertainties in the reconstruction. One approach to optimize the wavelengths is to have a greater set of denominators in equations [5], [9] and [10]. For the scattering aspect in equations [9] and [10], several random attempts show that the value of

$$\left| m\sum_{i=1}^{m} \log^2(\lambda_i) - \left[\sum_{i=1}^{m} \log(\lambda_i)\right]^2 \right|$$ stays in a narrow range of [0.1, 1].

However, for equation [5], the determinant of $\varepsilon^T\varepsilon$ varies in several orders depending upon the wavelengths, which is however not unexpected because the similarities between the row-vectors in matrix ε could induce rank deficiency. Corlu *et al.* (2, 8) and Eames *et al.* (22) indicated such issue of rank deficiency and recommended to construct the sensitivity matrix with small residual numbers. From another perspective, however, one could associate the determinant of a matrix with the area bounded by the row-vectors of the matrix. This suggests that maximizing the determinant of the matrix $\varepsilon^T\varepsilon$ will likely decrease the similarities among the row-vectors in the matrix ε and minimize its rank deficiency. The study in (22) also indicates that within the sensitivity matrix, less variation among the sub-matrices with respect
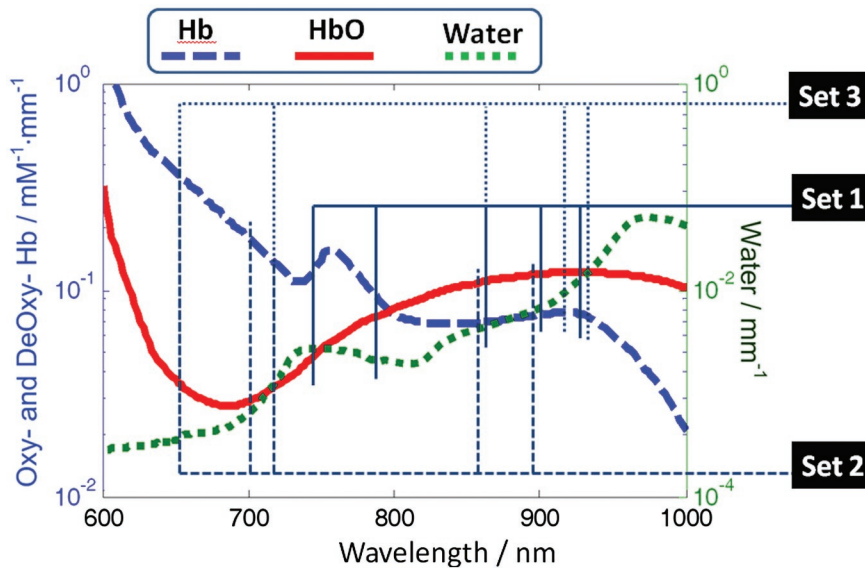

Figure 1: Illustration of the wavelength sets, which were used in an independent experimental study (8), employed for this study. The set 1 expands 186 nm from 740 nm to 926 nm. The set 2 expands 240 nm from 650 nm to 890 nm. The set 3 expands 280 nm from 650 nm to 930 nm. The spectra in Figure 1 follow the chromophore absorption spectra used in (2, 8), which are based on the same study by Prahl (23).

Table I
Wavelength sets to be examined and comparison of PRULs evaluation with the analytical solutions.

Sets	Wavelengths/nm	Absorption Part		Scattering Part	
		Determinant of denominator: $(\varepsilon^T \varepsilon)$	Standard deviation of extinction coefficients dev(ε)	Determinant of denominator	Standard deviation of $\partial x/\partial M(\lambda)$
(2)	650,700,716,860,890	2.58e-7	388.0	0.37	0.67
(1)	740,788,866,902,926	8.18e-7	63.7	0.18	1.03
(3)	650,716,866,914,930	1.30e-5	63.8	0.53	0.45

to each category of reconstruction parameters (such as chromophore concentrations and scattering parameters) renders more favorable reconstruction. This study thereby includes the magnitude uniformity of $\partial x/\partial M$ in equation (3) as one of the criteria for wavelength optimization.

Optimization methods in (2, 8, 20, 22) appraise the residue and condition numbers of sensitivity matrix that includes $n_{\text{source-detector-pair}} \times n_{\text{measurement-wavelength}} \times n_{\text{nodes}}$ terms. The method introduced in this study examines equations [5], [11] and [12], and the total evaluation number is $n_{\text{source-detector-pair}} \times n_{\text{measurement-wavelength}}$, which is n_{nodes} times less in the computation load needed than the methods introduced in (2, 8, 20, 22). Table I illustrates the outcome when applying our criteria to the three sets of spectral-*prior*, after neglecting the common terms $|\partial\mu(\lambda)/\partial M(\lambda)|\cdot\sigma_{M(\lambda)}$ in equation [3]. Since the optimization is in favor of large denominator of the determinant and small variation among the gradient values, the set 3 stands out as the best. The set 1 significantly outperforms the set 2 in absorption part, whereas the set 2 moderately outperforms the set 1 in scattering part. The overall ranking among the three sets of spectral-*prior* is thus (3, 1, 2), which agrees with the results in (8).

Quantitative Evaluations of Relative PRULs

To quantitatively evaluate the PRULs in equations [6], [11] and [12], we assign the background chromophore concentrations and scattering parameters as (22): $C_{\text{HbO}} = C_{\text{Hb}} = 0.01 \, \text{mM}$, $C_{\text{H2O}} = 40\%$ and $A = b = 1$. The preset properties of the anomaly are approximately two-folds of those assigned to the background, as: $C_{\text{HbO\_anom}} = 0.023 \, \text{mM}$, $C_{\text{Hb\_anom}} = 0.023 \, \text{mM}$, $C_{\text{H2O\_anom}} = 80\%$, $A_{\text{anom}} = 2$, and $b_{\text{anom}} = 2$. The relative uncertainties of all measurement differences are assumed as 1% (19), that is: $\frac{\sigma^2_{\delta(\lambda)}}{\delta^2(\lambda)} = \frac{\sigma^2_{a(\lambda)}}{a^2(\lambda)} = \frac{\sigma^2_{\phi(\lambda)}}{\phi^2(\lambda)} = (1\%)^2$. Besides, for the range of wavelengths and modulation frequency commonly utilized in optical tomography, one could approximate

$$\frac{a^2(\lambda) + \phi^2(\lambda)}{a^2(\lambda) - \phi^2(\lambda)} = \left(\sqrt{1 + \frac{\omega^2}{v^2 \mu_a^2(\lambda)}}\right) \text{ as 1. With these necessary}$$

pre-conditioning, Table II shows the quantitative evaluations of PRULs in equations [6], [11] and [12], and normalizes the

PRULs by the pre-set contrasts of the anomaly. Such normalized values relate to the Noise-to-Contrast Ratios (NCR) in the reconstruction. In Table II, the absolute NCRs are further normalized by those of DC-only in each column, the absorption part is further normalized by NCRs of the hemoglobin in each row, and the scattering part is normalized by NCRs of the scattering amplitude in each row. Such normalizations more explicitly indicate the rankings of NCR among three measurement conditions for each reconstruction parameter.

From the Row-wise Norm. in Table II, one would expect that DC reconstruction has the least NCRs and accordingly, the least relative uncertainties in the reconstruction. One would also expect that including DC measurements in FD at several cases does not necessarily increase the reconstruction NCRs. Based on the Column-wise Norm. in Tables II, one would also expect that for the three sets of wavelengths, $\text{NCR}_{\text{C\_Hb}} < \text{NCR}_{\text{C\_H2O}} < \text{NCR}_{\text{C\_HbO}}$ for the absorption aspect and $\text{NCR}_A < \text{NCR}_b$ for the scattering aspect.

Simulation Studies

Synthetic Model and Geometry

The synthetic study is based on NIRFAST package (24). The forward model computes photon diffusion at each wavelength by:

$$\left(-\frac{\mu_a(\vec{r}, \lambda)}{D(\vec{r}, \lambda)} + \frac{i\omega}{vD(\vec{r}, \lambda)}\right)U(\vec{r}, \omega, \lambda) + \nabla^2 U(\vec{r}, \omega, \lambda)$$
$$= -\frac{S(\vec{r}, \omega, \lambda)}{D(\vec{r})} \quad [16]$$

where $U(\vec{r}, \omega, \lambda)$ is the photon fluence of wavelength λ at frequency ω (for DC simply assigning $\omega = 0$) for position $\vec{r}$, and $S(\vec{r}, \omega, \lambda)$ is the source term. The Robin type boundary condition is assigned as:

$$U(\vec{r}_0, \omega) - 2DA\hat{n}_0 \cdot \nabla U(\vec{r}_0, \omega) = 0 \quad [17]$$

where $\vec{r}_0$ denotes the boundary node; A is the coefficient accounting for the refractive index mismatch; and $\hat{n}_0$ is the

Table II
Analytical evaluation of parameter reconstruction uncertainty levels normalized by target contrasts (NCRs).

		HbO/mM			Hb/mM			H$_2$O/%			A			b		
Sets	Measurement	Abs.	Column-wise Norm.	Row-wise Norm.	Abs.	Column-wise Norm.	Row-wise Norm.	Abs.	Column-wise Norm.	Row-wise Norm.	Abs.	Column-wise Norm.	Row-wise Norm.	Abs.	Column-wise Norm.	Row-wise Norm.
(1)	DC	0.044	1	2.0	0.022	1	1	0.030	1	1.4	0.010	1	1	0.053	1	5.2
	AC + PHS	0.062	1.41	2.0	0.031	1.41	1	0.042	1.41	1.4	0.015	1.41	1	0.075	1.41	5.2
	DC + AC + PHS	0.107	2.45	2.0	0.054	2.45	1	0.072	2.45	1.4	0.015	1.41	1	0.075	1.41	5.2
(2)	DC	0.127	1	9.4	0.014	1	1	0.126	1	9.3	0.011	1	1	0.037	1	3.3
	AC + PHS	0.180	1.41	9.4	0.019	1.41	1	0.179	1.41	9.3	0.016	1.41	1	0.052	1.41	3.3
	DC + AC + PHS	0.311	2.45	9.4	0.033	2.45	1	0.310	2.45	9.3	0.016	1.41	1	0.052	1.41	3.3
(3)	DC	0.054	1	5.4	0.010	1	1	0.032	1	3.2	0.008	1	1	0.031	1	3.9
	AC + PHS	0.076	1.41	5.4	0.014	1.41	1	0.046	1.41	3.2	0.011	1.41	1	0.044	1.41	3.9
	DC + AC + PHS	0.132	2.45	5.4	0.025	2.45	1	0.080	2.45	3.2	0.011	1.41	1	0.044	1.41	3.9

outgoing normal vector. The sensitivity or Jacobian matrix is constructed according to the measurands (18) as:

$$
J = \begin{bmatrix} DC \\ AC \\ PHS \end{bmatrix} = \begin{bmatrix} \dfrac{\partial \ln U_{DC}(\lambda_1)}{\partial x} & \dfrac{\partial \ln U_{DC}(\lambda_2)}{\partial x} & \cdots & \dfrac{\partial \ln U_{DC}(\lambda_m)}{\partial x} \\ \dfrac{\partial \ln |U_{AC}(\lambda_1)|}{\partial x} & \dfrac{\partial \ln |U_{AC}(\lambda_2)|}{\partial x} & \cdots & \dfrac{\partial \ln |U_{AC}(\lambda_m)|}{\partial x} \\ \dfrac{\partial \Phi_{AC}(\lambda_1)}{\partial x} & \dfrac{\partial \Phi_{AC}(\lambda_2)}{\partial x} & \cdots & \dfrac{\partial \Phi_{AC}(\lambda_m)}{\partial x} \end{bmatrix} \quad [18]
$$

where x represents the parameters to be reconstructed, including chromophore concentrations and scattering amplitude and scattering power.

Figure 2 shows a circular geometry with the medium enclosed by a ring-applicator of 86 mm in diameter (3, 18, 20, 22). 16 optodes are evenly distributed along the circumference, and each optode functions sequentially as the source with the other 15 optodes being the detection channels. As a two-dimensional optode array is simulated and all the targets are assumed centering on the plane of the optode array, two-dimensional finite-element-method (FEM) simulation is used in this study (25). The imaging geometry is discretized into 3418 finite-elements with 1785 nodes. All the simulations used 30 × 30 pixel basis for reconstruction. The reconstruction routines stop as the change of the projection error falls below 2%.

The optical properties employed in the simulations are identical to those used for Tables II, and an anomaly could have one or multiple contrasts of the properties. Two sets of simulations are conducted. One set simulates five targets with independent contrasts, and the other set studies two closely

positioned targets of identical properties. White noise at 1% is added to the forward data before applying the Levernberg-Marquardt algorithm as the inverse solver.

Simulation Results

Reconstructing Targets with Independent Contrasts

The set targets are five 8 mm-radius contrast-regions located 25 mm away from the center of the geometry with 0.4π angular separation, as shown in the column set of Figure 3. Each of the five regions differs from the rest
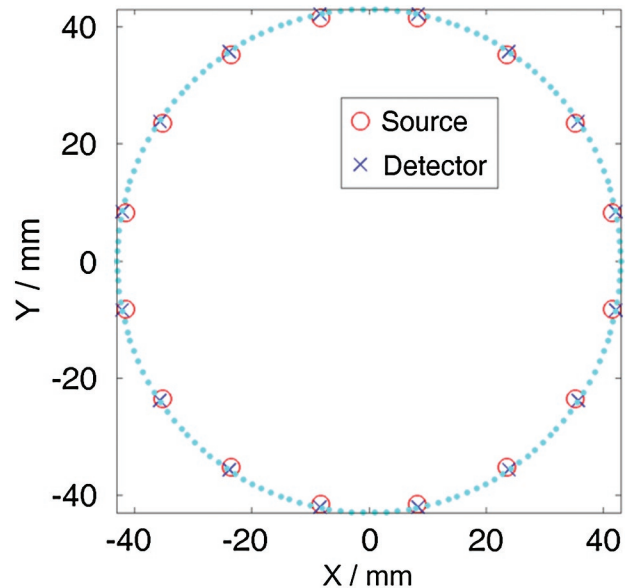

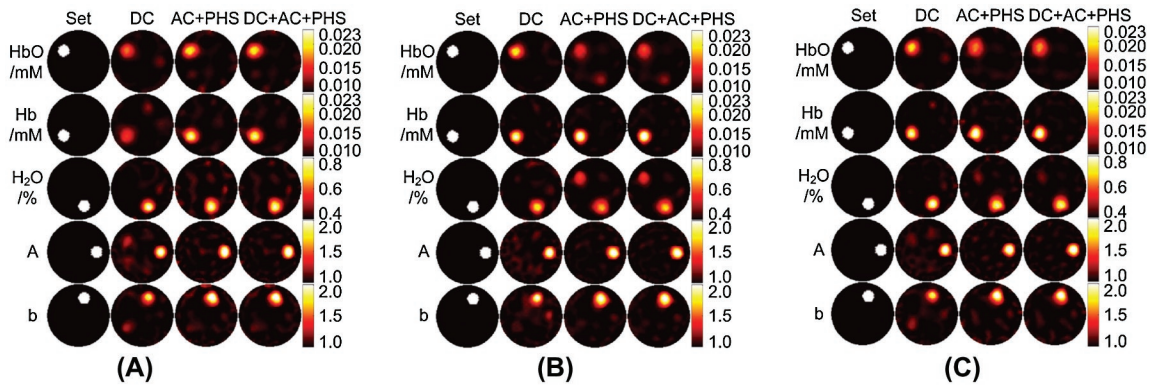**Figure 2:** Simulation geometry. The FEM mesh has a radius of 43 mm and includes 1785 nodes and 3418 elements.

Figure 3: Synthetic study on five targets with independent contrasts in image geometry shown in Figure 2. (**A**)(**B**)(**C**) are the results for the wavelength sets (1)(2)(3) in Table I, respectively. (**A**) Second best: slight cross-coupling between HbO/A and between Hb/b recovery in column DC. (**B**) Worst: Severe cross-coupling between HbO and H$_2$O. (**C**) Best: minimal cross-coupling and target underestimation. Note: target overestimation is not visible because of uniform color bars. Look for absolute values in Table III.

in its contrast. Figure 3 shows the reconstruction results for the three sets of spectral-*prior*, and Table III demonstrates the maximum values of each variable within the target regions and the percentage error of the contrast. In terms of the overall accuracy quantified in the Table III and the artifact visualized in the Figure 3, the set 3 shown in Figure 3(C) outperforms the other two. Next to the set 3 is the set 1 shown in Figure 3(A), wherein the DC reconstruction underestimates HbO and Hb yet overestimates A and b due to cross-coupling. The set 2 shown in Figure 3(B) is the least accurate, specifically in FD reconstruction, as it has the highest level of cross-coupling between the HbO and H$_2$O concentrations.

Table IV lists the NCRs of the reconstruction results in Figure 3, that is, the standard deviations (σ_x) of the reconstructed background values normalized by the maximum target contrasts. The σ_x values are calculated by excluding the

areas co-centric to the targets but with the radii twice as those of the target regions. Similar to those in Table II, the NCRs in Table IV are normalized by those of DC-only in each column. Similarly in each row of Table IV, the absorption part is normalized by NCRs of the Hb and the scattering part is normalized by NCRs of the A. The row-wisely normalized NCRs in Table IV unanimously show $NCR_{C\_Hb} < NCR_{C\_H2O} < NCR_{C\_HbO}$ for the absorption part and $NCR_A < NCR_b$ for the scattering part, which agree with those predicted in Table II. For column-wisely normalized NCRs, in the sets 1 and 3, both Table II and IV indicate that the ratio of AC + PHS over DC stays within the range of [1, 2]. The artifact levels of DC + AC + PHS reconstruction are shown always lower than those of AC + PHS and sometimes lower than those of DC. Similar observations were reported in (18), and collectively they conclude that DC component is indeed not-redundant in FD measurements, therefore neglecting DC would

Table III

Target accuracy in Figure 3.

	Data	HbO/mM		Hb/mM		H$_2$O/%		A		b	
		Abs.	Err./%	Abs.	Err./%	Abs.	Err./%	Abs.	Err./%	Abs.	Err./%
	Set Values	2.3e-2		2.3e-2		0.80		2.0		2.0	
	DC	1.7e-2	−46	1.6e-2	−55	0.82	5	2.2	21	1.9	−9
(1)	AC + PHS	2.0e-2	−23	2.3e-2	−2	0.81	2	2.4	39	2.3	30
	DC + AC + PHS	2.0e-2	−24	2.2e-2	−6	0.80	0.4	2.3	34	2.2	23
	DC	2.0e-2	−21	2.4e-2	4	0.72	−21	2.4	40	2.1	7
(2)	AC + PHS	1.6e-2	−56	2.6e-2	24	0.67	−33	2.3	26	2.1	6
	DC + AC + PHS	1.7e-2	−48	2.7e-2	27	0.69	−27	2.2	23	2.1	10
	DC	2.0e-2	−25	2.3e-2	1	0.83	8	2.3	33	1.9	−11
(3)	AC + PHS	1.8e-2	−42	2.5e-2	16	0.78	−6	2.4	45	2.2	19
	DC + AC + PHS	1.8e-2	−39	2.5e-2	18	0.77	−8	2.4	39	2.2	17

Table IV

Absolute and normalized NCRs of the images in Figure 3.

Sets	Measurement	HbO/mM Abs.	Column-wise Norm.	Row-wise Norm.	Hb/mM Abs.	Column-wise Norm.	Row-wise Norm.	H$_2$O/% Abs.	Column-wise Norm.	Row-wise Norm.	A Abs.	Column-wise Norm.	Row-wise Norm.	b Abs.	Column-wise Norm.	Row-wise Norm.
	DC	0.066	1	1.3	0.052	1	1	0.039	1	0.7	0.022	1	1	0.051	1	2.3
(1)	AC + PHS	0.072	1.6	2.1	0.035	1.4	1	0.066	1.7	1.9	0.038	2.0	1	0.057	1.6	1.5
	DC + AC + PHS	0.058	1.2	1.8	0.033	1.3	1	0.049	1.2	1.5	0.032	1.6	1	0.047	1.3	1.4
	DC	0.048	1	1.4	0.033	1	1	0.063	1	1.9	0.028	1	1	0.043	1	1.5
(2)	AC + PHS	0.054	0.6	2.2	0.025	0.9	1	0.049	0.7	2.0	0.025	0.8	1	0.037	0.9	1.5
	DC + AC + PHS	0.049	0.7	2.1	0.023	0.9	1	0.047	0.7	2.0	0.027	0.8	1	0.036	0.9	1.3
	DC	0.049	1	1.9	0.026	1	1	0.040	1	1.5	0.026	1	1	0.038	1	1.5
(3)	AC + PHS	0.072	1.1	1.6	0.044	2.0	1	0.047	1.0	1.1	0.024	1.0	1	0.050	1.8	2.1
	DC + AC + PHS	0.052	0.9	1.6	0.033	1.5	1	0.037	0.8	1.1	0.020	0.8	1	0.040	1.4	2.0

degrade the accuracy of FD reconstruction. In the set 2, the NCRs are slightly lower in FD than in DC-only. This implies that FD measurement is more robust in case of less desirable spectral-*prior*.

Resolving Two Closely Positioned Identical Targets

In Figure 4, two identical targets of 8-mm in radius are embedded 25 mm from the center and the angular separation between the targets is $\pi/4$. Each target has all five contrast properties as previously defined. Figure 4 indicates that DC seems to be comparable to FD in the estimation of Hb, A, and b, but underestimates the concentration of Hb and H$_2$O as comparing to FD. To explicitly compare how well the targets are resolved, the parameter contours along the concentric circle of the imaging geometry and across the targets (marked with gold dotted loops in Figure 4) are plotted in Figure 5.

Figures 4 and 5 show that even though the absolute properties of the target are the least accurate in DC reconstruction, the two targets are seemed better resolved in DC than in FD. Table V lists the ratios of target-to-valley contrast over target-to-background contrast (both contrasts are illustrated in the upper-left subfigure of Figure 5). Larger ratios indicate better identification of the targets. It is shown that, except for the cases of possessing the contrast of "A", the targets are always resolved more clearly in DC than in FD.

Comparison of $\mu_a(\lambda)$ and $\mu_s'(\lambda)$

Since the sensitivity matrices of multi-spectral NIR tomography are derived from that of single-wavelength optical tomography, the reconstruction results of $\mu_a(\lambda)$ and $\mu_s'(\lambda)$ could also be insightful to the evaluation of the reconstruction performance. In this section, the analytical model of
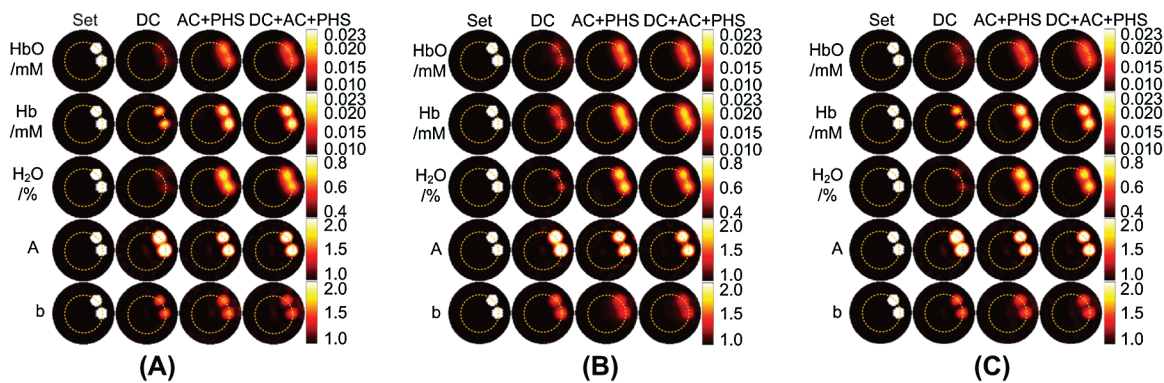

Figure 4: Synthetic study on two targets with all five parameter contrasts in image geometry shown in Figure 2. (**A**)(**B**)(**C**) are the results for the wavelength sets (1)(2)(3) in Table I, respectively. Cross-coupling are severe in all reconstructed parameters. (**A**) Second best: targets are inseparable in H$_2$O distribution recovery by FD reconstructions. (**B**) Worst: targets are inseparable in Hb and b distribution recovery by FD reconstructions. (**C**) Best: targets are separated in all cases.
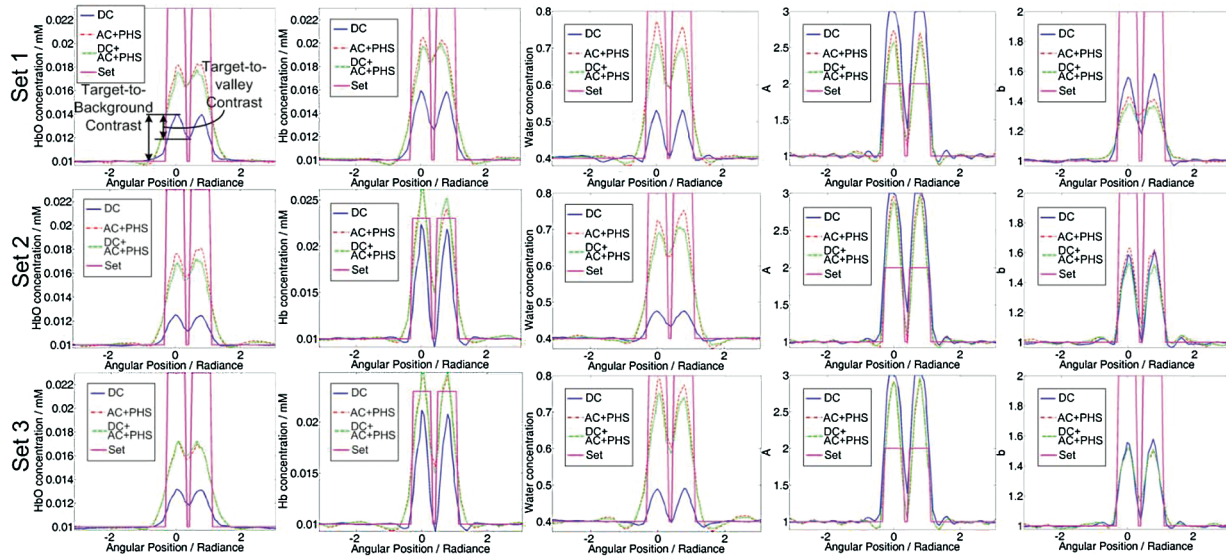
Figure 5: Parameter contour plots along the gold dash lines in Figure 4. The upper left subfigure denotes the target-to-valley contrast and target-to-background contrast. DC reconstruction shows relatively deeper contrast valleys between the targets for most cases.

$\sigma_{\mu a(\lambda)}$ and $\sigma_{\mu s'(\lambda)}$ will be compared to $\sigma_{\mu a(\lambda)}$ and $\sigma_{\mu s'(\lambda)}$ derived from synthetic studies. However, there is difference between the PRUL calculations of $\sigma_{\mu a(\lambda)}$ and $\sigma_{\mu s'(\lambda)}$ in analytical model and in simulation. For analytical model, the calculations of $\sigma_{\mu a(\lambda)}$ and $\sigma_{\mu s'(\lambda)}$ involve evaluating $\mu_a(\lambda)$ and $\mu_s'(\lambda)$ in equation [2] with the preset simulation parameters and substituting $\mu_a(\lambda)$ and $\mu_s'(\lambda)$ values into Table II and IV in (18). Whereas for simulation, $\mu_a(\lambda)$ and $\mu_s'(\lambda)$ values are not recovered explicitly in the reconstruction under spectral-*prior*,

Table V

Comparison of target separation in Figure 5.

	Data	HbO	Hb	H$_2$O	A	b
	DC	0.76	0.56	0.98	0.81	0.68
(1)	AC + PHS	0.15	0.18	0.47	0.93	0.27
	DC + AC + PHS	0.36	0.15	0.35	0.87	0.30
	DC	0.54	1.07	0.57	0.80	1.01
(2)	AC + PHS	0.25	0.65	0.31	1.01	0.80
	DC + AC + PHS	0.20	0.67	0.21	0.97	0.85
	DC	0.42	1.06	1.01	0.81	0.93
(3)	AC + PHS	0.19	0.61	0.46	0.99	0.67
	DC + AC + PHS	0.18	0.66	0.52	0.99	0.70

Note: Data are calculated as the ratio of the target-to-valley contrast over target-to-background contrast (target-to-valley contrast over and target-to-background contrast are illustrated respectively, in Figure 5 subfigure Set 1, Column HbO).
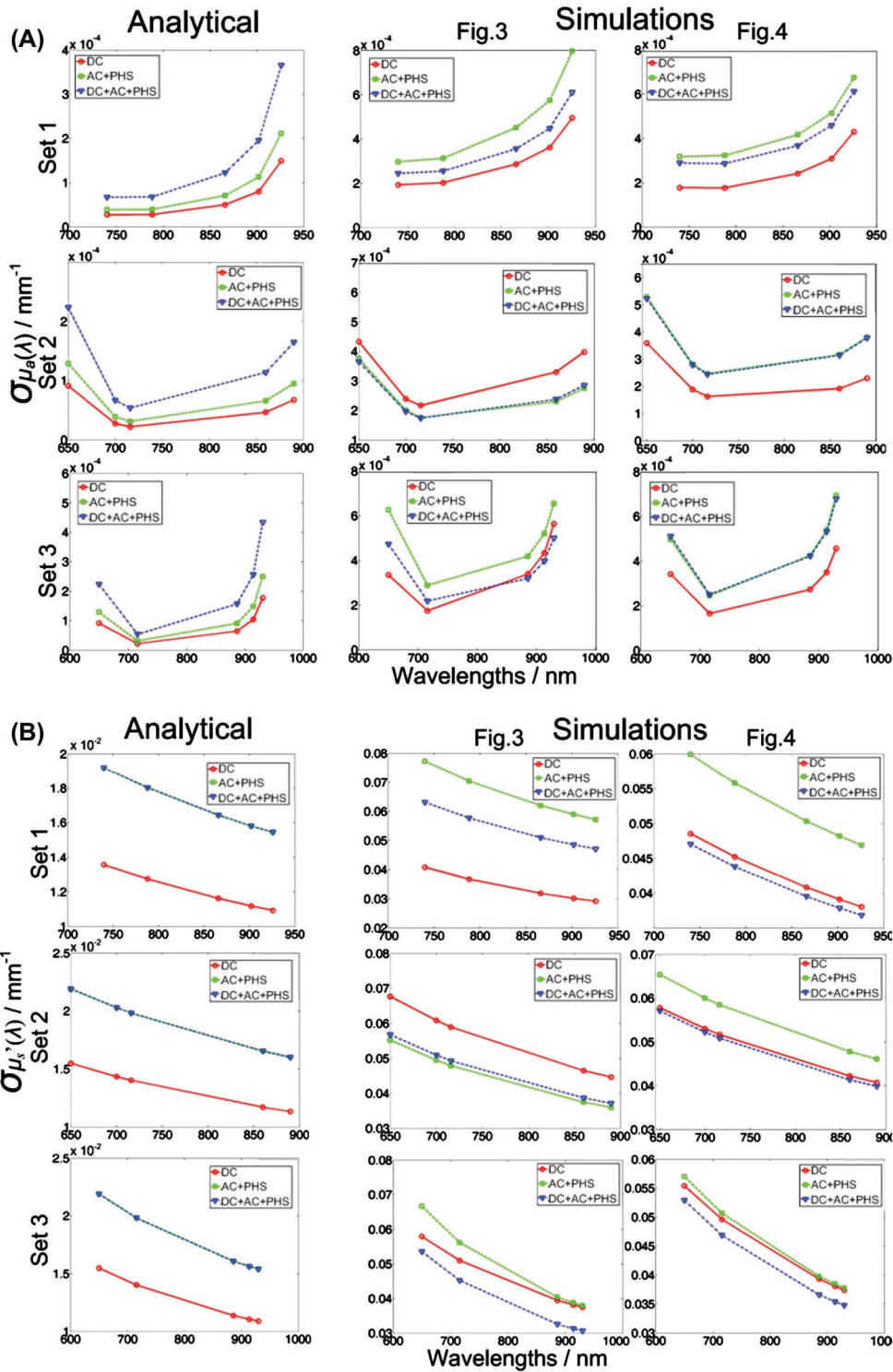
therefore, the PRULs of the recovered parameters need to be reversely projected to $\sigma_{\mu a(\lambda)}$ and $\sigma_{\mu s'(\lambda)}$, by:

$$\left(\vec{\sigma}_{\bar{\mu}_a(\lambda)}\right)_{m\times 1} = \left|\frac{\partial \vec{\mu}_a(\lambda)_{m\times 1}}{\partial(\vec{c})_{n\times 1}}\right|_{m\times n} \times (\vec{\sigma}_c)_{n\times 1} \qquad [19]$$

$$= \log(10)\cdot(\vec{\varepsilon})_{m\times n}\times(\vec{\sigma}_c)_{n\times 1}$$

and

$$\left(\sigma_{\mu_s'(\lambda)}\right)_{m\times 1} = \sqrt{\left(\frac{\partial \mu_s'(\lambda)}{\partial A}\right)_{m\times 1}^2 \cdot \sigma_A^2 + \left(\frac{\partial \mu_s'(\lambda)}{\partial b}\right)_{m\times 1}^2 \cdot \sigma_b^2}$$

$$= \left(\sqrt{(\lambda^{-b}\cdot \sigma_A)^2 + (-A\lambda^{-b}\cdot \log \lambda \cdot \sigma_b)^2}\right)_{m\times 1} \qquad [20]$$

Analytical and simulated values of $\sigma_{\mu a}(\lambda)$ and $\sigma_{\mu s'}(\lambda)$ are plotted verses the wavelengths in Figure 6 (A) and (B) respectively. The curve shapes agree between the analytical predictions and reconstruction results, yet the relative magnitudes of the curves differ slightly. In the analytical prediction, the uncertainties always follow the relationship of $\sigma_{DC} < \sigma_{AC+PHS} \leq \sigma_{DC+AC+PHS}$ for both $\mu_a(\lambda)$ and $\mu_s'(\lambda)$. In simulation study, one has $\sigma_{\mu a(\lambda)\_DC} < \sigma_{\mu a(\lambda)\_DC+AC+PHS} \leq \sigma_{\mu a(\lambda)\_AC+PHS}$. However, for $\sigma_{\mu s'}(\lambda)$ in Figure 6 (B), DC reconstruction is not always advantageous than FD. Such outcome is in no doubt related to the phase information residing in FD as that gives an additional dimension to unveil the separate contributions of $\mu_a(\lambda)$ and $\mu_s'(\lambda)$ to the photon fluence. When phase information is employed, however, $\sigma_{\mu s'(\lambda)\_DC+AC+PHS} < \sigma_{\mu s'(\lambda)\_AC+PHS}$ stands for all cases, indicating that DC information is not redundant in FD.

Figure 6: Comparison between the artifact levels in absorption and scattering coefficients at each wavelength. Curve shapes of analytical model and synthetic studies agree in all cases. (**A**) Absorption coefficients comparison. DC reconstructions show least background artifact levels. DC + AC + PHS at most cases outperforms AC + PHS. (**B**) Scattering coefficients comparison. DC reconstructions does not necessarily show least background artifact levels. DC + AC + PHS at most cases outperforms AC + PHS.

Discussions

The analytical model is derived under the condition of infinite medium, in which the measurements defined in equation [1] are linear with respect to ρ. However, the circular imaging geometry possesses a boundary and can be approximated at best as a semi-infinite medium. The solution of photon diffusion in a semi-infinite geometry generally utilizes an image source with respect of an extrapolated boundary (26). Boas derived an approximation solution to photon diffusion in the semi-infinite geometry in (27) under the condition that the source-detector distance is much larger than the diffusion path length. The equation is rewritten following the notations of this study:

$$U(\vec{r},\omega) = \frac{vS(\vec{r}',\omega)e^{ikd}}{4\pi Dd^2}\left[-4ik(z_b^2 + z_b z_{tr})\right] \qquad [21]$$

where ω is the angular modulation frequency, $U(\vec{r},\omega)$ is the photon fluence detected at position $\vec{r}$, $S(\vec{r}',\omega)$ is the light source at $\vec{r}'$, $d = |\vec{r}' - \vec{r}|$ is source-detector distance, z_b is the distance of the extrapolated boundary to the physical boundary, $z_{tr} = (\mu_s')^{-1}$ is the diffusion path length, and k is the wave number of the photon fluence:

$$k_{CW} = ik_{DC} \qquad [22\text{-}CW]$$

$$k_{FD} = ik_{AC} - k_{PHS} \qquad [22\text{-}FD]$$

where k_{DC} k_{AC} and k_{PHS} are defined in equation [1]. Note that the factor $\left[-4ik(z_b^2 + z_b z_{tr})\right]$ in [21] is constant, therefore one has the following linear relationship between $\log\left[d^2 \cdot U(\vec{r},\omega)\right]$ and d:

$$\log[d^2 \cdot U_{CW,FD}(\vec{r},\omega)] = ik_{CW,FD}d + \log\left(\frac{vS(\vec{r}',\omega)}{4\pi D}\right) \\ + \log[-4ik_{CW,FD}(z_b^2 + z_b z_{tr})] \qquad [23]$$

Following equation [1] we define the difference between $\ln(d^2 \cdot U(d))$ measured at d_1 and d_2 away from the source as:

$$\delta = \log[d_1^2 \cdot U_{CW}(d_1)] - \log[d_2^2 \cdot U_{CW}(d_2)] \qquad [24\text{-}CW]$$
$$= \left|d_1 - d_2\right| \cdot ik_{CW} = -\rho \cdot k_{DC}$$

$$a + i\phi = \log[d_1^2 \cdot U_{FD}(d_1)] - \log[d_2^2 \cdot U_{FD}(d_2)] \qquad [24\text{-}FD]$$
$$= \left|d_1 - d_2\right| \cdot ik_{FD} = -\rho \cdot k_{AC} + \rho \cdot ik_{PHS}$$

and the expressions of δ, a and ϕ are consistent with those in equation [1] and [24]. Therefore, the outcomes derived under infinite medium conditions are applicable to geometries with semi-infinite boundaries.

The PRUL analyses introduced in (18) actually implicated the uniqueness of the solutions of DC only reconstruction in multi-spectral NIR tomography. Previous studies (28-29) suggested that in a homogenous medium, the product of $\mu_a(\lambda)$ and $D(\lambda)$ can be considered as a constant function of the surface diffuse reflectance of the medium as:

$$[\mu_a \cdot D] = K(R_\infty) \qquad [25]$$

Taking equation [25] into consideration, $\mu_a(\lambda)$, $D(\lambda)$ and $\mu_s'(\lambda)$ can be independently expressed as (18):

$$\mu_a(\lambda)\big|_{DC} = \sqrt{K(R_\infty(\lambda))} \cdot \frac{\delta(\lambda)}{\rho} \qquad [26.1]$$

$$D(\lambda)\big|_{DC} = \sqrt{K(R_\infty(\lambda))} \cdot \frac{\rho}{\delta(\lambda)} \qquad [26.2]$$

$$\mu_s'(\lambda)\big|_{DC} = \frac{1}{(3D(\lambda))} - \mu_a(\lambda)\big|_{DC}$$
$$= \left(\frac{1}{3\sqrt{K(R_\infty(\lambda))}} - \sqrt{K(R_\infty(\lambda))}\right) \cdot \frac{\delta(\lambda)}{\rho} \qquad [26.3]$$

If the DC optical tomography measurement lacks $K(R_\infty)$, equation [26] may become under-determined and thereby inter-parameter cross-coupling may exist. Under spectral-*prior*, however, the $\sqrt{K(R_\infty(\lambda))}$ term could be eliminated and subsequently the cross-coupling be reduced. By combining equations [26.1] and [26.3] and substituting into equations [2-μ_a] and [2-μ_s'], the DC measurement becomes the function of only the absorption chromophore concentrations and scattering parameters as:

$$\frac{\delta^2(\lambda)}{\rho^2} = 3\mu_a(\lambda)(\mu_a(\lambda) + \mu_s'(\lambda)) \qquad [27]$$
$$= 3 \cdot \sum_i \varepsilon_i(\lambda)c_i \cdot \left(\sum_i \varepsilon_i(\lambda)c_i + A\lambda^{-b}\right)$$

Therefore one can decouple the unknown values once measurements at sufficient number of wavelengths are available. This agrees with the observation in this and several previous studies that DC reconstruction with spectral-*prior* successfully resolves the target, as evidenced in Figures 3. Interestingly, as is shown in Figures 4, even in the FD reconstruction the intrinsic cross-coupling problem becomes significant when multiple contrasts are assigned to the same location (21). As fewer measurement components in DC reconstruction facilitate less system noise in the inverse problem, the level of background artifacts could actually be lower in DC reconstruction.

The PRUL analyses of both multi-spectral reconstruction parameters and the optical properties have been shown reliable. The method of ranking the spectral-*prior* based on PRUL sets conforms to the recommendation by (8) at desirably less computation load. However, there is still disagreement between the analytical prediction and simulation results due to the approximation in analytic modeling and smoothing effect in synthetic studies. For example, since the analytical model only accounts for the perturbations in the measurement, it is predicted that DC-excluded FD will outperform DC-included FD, yet the simulation shows the contrary. Such aberrations actually explain that extra information in DC components has balanced the excessive reconstruction uncertainties and made DC + AC + PHS a better choice than AC + PHS for FD reconstruction.

Using the three sets of wavelengths experimented in an independent prior work, this study investigated two aspects of the spectral *prior*: (1) for a given spectral *prior*, which among the chromophore concentrations (HbO, Hb, and H_2O) or between the scattering properties (A and b) is recovered at lower (hence better) noise-to-contrast-ratio, regardless of using DC or FD reconstruction; (2) for a given spectral *prior*, which measurement information among DC, DC-excluded FD, and DC-included FD leads to better quantification or resolution of the target(s).

For the first above-mentioned aspect of spectral *prior*, it is shown, from both numerical estimation based on the introduced analytical approach and simulation, that the rank of overall quality of chromophore recovery is Hb, H_2O, and HbO from the highest to lowest; and in the scattering part the A is always better recovered than b. This finding, on the other hand, demonstrates that the DC-only information results in unique solution to the image reconstruction routine, under adequate (not necessarily optimal) spectral *prior*.

The second above-mentioned aspect of spectral *prior* actually gives rise to two important observations that were not widely appreciated previously: whether DC information is redundant in FD reconstruction, and how DC-only reconstruction compares with DC-excluded or DC-included FD reconstruction. It is shown in this study that, the artifact levels of DC + AC + PHS, or DC-included FD, reconstruction are always lower than those of AC + PHS, or DC-excluded FD. Therefore one should expect that the DC component is indeed not-redundant in FD measurements, and neglecting DC degrades the contrast-to-noise-ratio of FD reconstruction. In terms of DC-only reconstruction versus FD reconstruction (including DC-excluded or DC-included), the DC-only does lead to less accurate quantification of the absolute investigated properties of the target comparing to what FD provides. However, multiple targets of identical contrasts over the background are resolved almost always more clearly by DC-only

than by FD reconstruction, except for the targets possessing the contrast of "A". Such salient features owe to the least level of artifacts in DC-only reconstruction associated with an optimal spectral *prior*, similar to what was demonstrated with single-band reconstruction (18). In the case of a less desirable spectral-*prior*, however, the FD could outperform DC in the recovery of scattering properties including both A and b, implying that the addition of phase-information helps the less desirable spectral *prior* resolve the scattering properties more robustly.

Conclusions

A PRUL analysis model has been applied to multispectral optical tomography and used to evaluate the outcome of three sets of wavelength for spectrally-constrained optical tomography reconstruction. Simulations in an external-imaging geometry are conducted to appraise the predictions given by the introduced analytical methods. Both numerical and simulation analyses demonstrate that the rank of overall quality of chromophore recovery is Hb, H_2O, and HbO from the highest to lowest; and in the scattering part the A is always better recovered than b. The DC-only information gives rise to unique solution to the image reconstruction routine under the given spectral *prior*. It is further shown that, DC-information is beneficial to FD-reconstruction, as the artifact levels of DC + AC + PHS, or DC-included FD, reconstruction are always lower than those of AC + PHS, or DC-excluded FD. The artifacts level as represented by the noise-to-contrast-ratio is almost always the least in DC-only, leading to generally better resolution of multiple targets of identical contrasts over the background than in FD. However, FD could outperform DC in the recovery of scattering properties including both A and b when the spectral *prior* is less optimal, implying the benefit of phase-information in scattering recovery in the context of spectrally-constrained optical tomography.

Acknowledgements

References

1. Tromberg, B. J., Pogue, B. W., Paulsen, K. D., Yodh, A. G., Boas, D. A., Cerussi, A. E. Assessing the future of diffuse optical imaging technologies for breast cancer management. *Medical Physics 35*, 2443-2451 (2008).
2. Corlu, A., Durduran, T., Choe, R., Schweiger, M., Hillman, E. M. C., Arridge, S. R., Yodh, A. G. Uniqueness and wavelength optimization in continuous-wave multispectral diffuse optical tomography. *Opt Lett 28*, 2339-2341 (2003).
3. Srinivasan, S., Pogue, B. W., Jiang, S., Dehghani, H., Paulsen, K. D. Spectrally constrained chromophore and scattering near-infrared

tomography provides quantitative and robust reconstruction. *Appl Opt 44*, 1858-1869 (2005).

4. Li, A., Zhang, Q., Culver, J. P., Miller, E. L., Boas, D. A. Reconstructing chromosphere concentration images directly by continuous-wave diffuse optical tomography. *Opt Lett 29*, 256-258 (2004).

5. Jobsis, F. F. Noninvasive, infrared monitoring of cerebral and myocardial oxygen sufficiency and circulatory parameters. *Science 198*, 1264-1267 (1977).

6. Bastian, H. On uniqueness in diffuse optical tomography. *Inverse Problems 25*, 055010 (2009).

7. Arridge, S. R., Lionheart, W. R. B. Nonuniqueness in diffusion-based optical tomography. *Opt Lett 23*, 882-884 (1998).

8. Corlu, A., Choe, R., Durduran, T., Lee, K., Schweiger, M., Arridge, S. R., Hillman, E. M. C., Yodh, A. G. Diffuse optical tomography with spectral constraints and wavelength optimization. *Appl Opt 44*, 2082-2093 (2005).

9. McBride, T. O., Pogue, B. W., Poplack, S., Soho, S., Wells, W. A., Jiang, S., Osterberg, U. L., Paulsen, K. D. Multispectral near-infrared tomography: a case study in compensating for water and lipid content in hemoglobin imaging of the breast. *Journal of Biomedical Optics 7*, 72-79 (2002).

10. Jiang, Z., Piao, D., Holyoak, G. R., Ritchey, J. W., Bartels, K. E., Slobodov, G., Bunting, C. F., Krasinski, J. S. Trans-rectal Ultrasound-coupled Spectral Optical Tomography of Total Hemoglobin Concentration Enhances Assessment of the Laterality and Progression of a Transmissible Venereal Tumor in Canine Prostate. *Urology 77*, 237-242 (2011).

11. Jones, P. B., Shin, H. K., Boas, D. A., Hyman, B. T., Moskowitz, M. A., Ayata, C., Dunn, A. K. Simultaneous multispectral reflectance imaging and laser speckle flowmetry of cerebral blood flow and oxygen metabolism in focal cerebral ischemia. *Journal of Biomedical Optics 13*, 044007 (2008).

12. Xu, H., Springett, R., Dehghani, H., Pogue, B. W., Paulsen, K. D., Dunn, J. F. Magnetic-resonance-imaging-coupled broadband near-infrared tomography system for small animal brain studies. *Appl Opt 44*, 2177-2188 (2005).

13. Brooksby, B., Srinivasan, S., Jiang, S., Dehghani, H., Pogue, B. W., Paulsen, K. D., Weaver, J., Kogel, C., Poplack, S. P. Spectral priors improve near-infrared diffuse tomography more than spatial priors. *Opt Lett 30*, 1968-1970 (2005).

14. Wang, J., Davis, S. C., Srinivasan, S., Jiang, S., Pogue, B. W., Paulsen, K. D. Spectral tomography with diffuse near-infrared light: inclusion of broadband frequency domain spectral data. *Journal of Biomedical Optics 13*, 041305-041310 (2008).

15. Wang, J., Jiang, S., Paulsen, K. D., Pogue, B. W. Broadband frequency-domain near-infrared spectral tomography using a mode-locked Ti:sapphire laser. *Appl Opt 48*, D198-D207 (2009).

16. Wang, J., Pogue, B. W., Jiang, S., Paulsen, K. D. Near-infrared tomography of breast cancer hemoglobin, water, lipid, and scattering using combined frequency domain and cw measurement. *Opt Lett 35*, 82-84 (2010).

17. Wang, J., Jiang, S., Li, Z., diFlorio-Alexander, R. M., Barth, R. J., Kaufman, P. A., Pogue, B. W., Paulsen, K. D. *In vivo* quantitative imaging of normal and cancerous breast tissue using broadband diffuse optical tomography. *Medical Physics 37*, 3715-3724 (2010).

18. Xu, G., Piao, D., Bunting, C. F., Dehghani, H. Direct-current-based image reconstruction versus direct-current included or excluded frequency-domain reconstruction in diffuse optical tomography. *Appl Opt 49*, 3059-3070 (2010).

19. Fantini, S., Franceschini, M., Fishkin, J. B., Barbieri, B., Gratton, E. Quantitative determination of the absorption spectra of chromophores in strongly scattering media: a light-emitting-diode based technique. *Appl Opt 33*, 5204-5213 (1994).

20. Eames, M. E., Wang, J., Pogue, B. W., Dehghani, H. Wavelength band optimization in spectral near-infrared optical tomography improves accuracy while reducing data acquisition and computational burden. *Journal of Biomedical Optics 13*, 054037-054039 (2008).

21. Li, C., Grobmyer, S. R., Chen, L., Zhang, Q., Fajardo, L. L., Jiang, H. Multispectral diffuse optical tomography with absorption and scattering spectral constraints. *Appl Opt 46*, 8229-8236 (2007).

22. Eames, M. E., Dehghani, H. Wavelength dependence of sensitivity in spectral diffuse optical imaging: effect of normalization on image reconstruction. *Opt Express 16*, 17780-17791 (2008).

23. Prahl, S. A. Optical absorption of hemoglobin. *http://omlc.ogi.edu/spectra/hemoglobin/* (1999). Accessed on May 22, 2011.

24. Dehghani, H., Eames, M. E., Yalavarthy, P. K., Davis, S. C., Srinivasan, S., Carpenter, C. M., Pogue, B. W., Paulsen, K. D. Near infrared optical tomography using NIRFAST: Algorithm for numerical model and image reconstruction. *Communications in Numerical Methods in Engineering 25*, 711-732 (2009).

25. Hebden, J. C., Veenstra, H., Dehghani, H., Hillman, E. M. C., Schweiger, M., Arridge, S. R., Delpy, D. T. Three-dimensional time-resolved optical tomography of a conical breast phantom. *Appl Opt 40*, 3278-3287 (2001).

26. Fantini, S., Franceschini, M. A., Gratton, E. Semi-infinite-geometry boundary problem for light migration in highly scattering media: a frequency-domain study in the diffusion approximation. *J Opt Soc Am B 11*, 2128-2138 (1994).

27. Boas, D. A. Diffusion photon probes of structral and dynamical properties of turbid media: theory and biomedical applications. *Ph.D dissertation* (University of Pennsylvania, Philadelphia, Pennsylvania, 2000).

28. Jacques, S. L. Reflectance spectroscopy with optical fiber devices and transcutaneous bilirubinometers. *Biomedical Optical Instrumentation and Laser-Assisted Biotechnology 12* (1996).

29. Fabbri, F., Franceschini, M. A., Fantini, S. Characterization of Spatial and Temporal Variations in the Optical Properties of Tissuelike Media with Diffuse Reflectance Imaging. *Appl Opt 42*, 3063-3072 (2003).